Validation of pore network simulations of ex-situ water distributions in a gas diffusion layer of proton exchange membrane fuel cells with X-ray tomographic images

Tristan Agaesse, Adrien Lamibrac, Felix N. Büchi, Joël Pauchet, Marc Prat

Validation of pore network simulations of ex-situ water distributions in a gas diffusion layer of proton exchange membrane fuel cells with X-ray tomographic images

Tristan Agaesse [a], Adrien Lamibrac [d], Felix N. Büchi [d], Joel Pauchet [a], Marc Prat [b, c, *]

[a] CEA, LITEN, LCPEM, F-38054 Grenoble, France
[b] Université de Toulouse, INPT, UPS, IMFT, Avenue Camille Soula, F-31400 Toulouse, France
[c] CNRS, IMFT, F-31400 Toulouse, France
[d] Electrochemistry Laboratory, Paul Scherrer Institut, CH-5232 Villigen PSI, Switzerland

HIGHLIGHTS

- X-ray tomographic images of liquid water in a GDL are compared to simulations.
- Pore network and full morphology simulations reproduced well the water distribution.
- Pore network extraction parameters were benchmarked using full morphology.

GRAPHICAL ABSTRACT

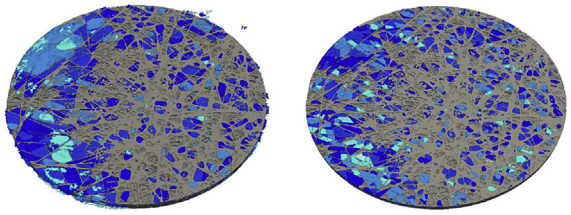

ABSTRACT

Understanding and modeling two-phase flows in the gas diffusion layer (GDL) of proton exchange membrane fuel cells are important in order to improve fuel cells performance. They are scientifically challenging because of the peculiarities of GDLs microstructures. In the present work, simulations on a pore network model are compared to X-ray tomographic images of water distributions during an ex-situ water invasion experiment. A method based on watershed segmentation was developed to extract a pore network from the 3D segmented image of the dry GDL. Pore network modeling and a full morphology model were then used to perform two-phase simulations and compared to the experimental data. The results show good agreement between experimental and simulated microscopic water distributions. Pore network extraction parameters were also benchmarked using the experimental data and results from full morphology simulations.

Keywords:
Polymer electrolyte membrane fuel cell
Gas diffusion layer
X-ray tomographic microscopy
Pore network
Full morphology
Liquid water

1. Introduction

Water management is a crucial aspect of Polymer Electrolyte Membrane Fuel Cells (PEMFC) operation. Water produced in excess by the oxygen reduction reaction needs to be removed from the cell to prevent flooding while the polymer membrane must stay well

* Corresponding author. Université de Toulouse, INPT, UPS, IMFT, Avenue Camille Soula, F-31400 Toulouse, France.
E-mail addresses: felix.buechi@psi.ch (F.N. Büchi), Joel.pauchet@cea.fr (J. Pauchet), mprat@imft.fr (M. Prat).

http://dx.doi.org/10.1016/j.jpowsour.2016.09.076

hydrated to conduct protons. Gas diffusion layers (GDL) are one of the electrodes porous layers [1] and a key component with respect to the water management. During fuel cell operation, liquid water can also appear in GDLs as a result of condensation [2]. Its effect is to impede the gas flux towards the catalyst layer where the electrochemical reactions take place, decreasing the fuel cell performance. The biphasic, electrical, thermal and mechanical behaviors of GDLs must be therefore understood and well characterized in order to optimize fuel cell performance. In this respect, it is desirable to develop efficient and accurate numerical tools to simulate two-phase flows in GDLs.

Biphasic simulations in PEMFCs porous media have been widely investigated [3,4]. The simulation methods can be divided into direct methods such as Lattice-Boltzmann and (mesoscale) geometry based methods like the full morphology [5] and pore networks models [6–8]. Mesoscale methods are preferred here in order to keep the computational cost low to allow for using images large enough to be representative of the GDL structure. It should be noted that the pore network models (PNM) have been frequently used to investigate two-phase flows in GDL, e.g. Refs. [2,9–22]. Therefore, it is particularly important to confirm that PNM are well adapted to describe two-phase flows in fibrous materials, especially for the case of the capillarity driven regime that is expected to prevail in GDLs [9]. This is not obvious a priori because the microstructure of fibrous materials is quite different from the structure of granular materials or porous rocks mostly considered in previous applications of PNM, e.g. Refs. [23,24].

It is usual to distinguish the structured pore networks from the unstructured ones. A structured pore network is constructed on a given lattice, typically a cubic lattice for 3D simulations. The pores are located on the nodes of the lattice and connected by narrower channels, also referred to as links, corresponding to the constrictions of the pore space. In a simple cubic network the channels are aligned with the three main directions of a Cartesian coordinate system. By, contrast, the unstructured networks offer the possibility to respect much more closely the local geometry of a given microstructure. Starting from a digital image of the "real" microstructure, the network is directly constructed from the image using appropriate numerical techniques. It is the approach taken in the present paper.

In this context, the main objective of the present paper is to investigate the capabilities of image based unstructured pore network and full morphology models to predict water distributions in fibrous materials such as the ones used in GDL. These simulation methods have already been successfully used to predict capillary pressure curves and saturation levels, e.g. Ref. [10] where a simple structured cubic network is used. The novelty in the present effort is to develop an image based unstructured pore network and to look at the three dimensional water distributions and not only to slice averaged saturation levels.

Extracting an unstructured pore network from a 3D digital image of a microstructure is described in a number of publications [25–29]. Most methods are based on medial axis analysis or the consideration of maximal balls. Several articles reviewed and discussed these methods [30–33]. As far as we are concerned, we develop a method based on watershed segmentation. Watershed segmentation [34,35] or similar methods [36,37] are used in several articles as an image analysis tool to segment pores without doing pore network extraction [38–40]. Recently a few approaches use watershed segmentation or similar methods as part of a pore network extraction procedure [26,28,29,41,42]. The principle of watershed segmentation is to find constrictions, defined in a robust way as watershed lines. It has several advantages: it is a well-known tool in image analysis, it is robust and off-the-shell open source codes are available. It also offers an explicit degree of freedom regarding the pore merging, thanks to pore markers defined by the user.

In order to validate our pore network extraction procedure and to study the impact of the pore merging degree of freedom, we compare pore network simulations with experimental data and full morphology simulations. Full morphology simulations are in fact suggested as a useful benchmark to test pore network extraction procedures.

The experimental data are 3D microscopic liquid water distributions from water injection experiments obtained by X-ray tomographic microscopy [11]. X-ray tomography has been used in several works to visualize liquid water in GDLs [23,24,43–49]. Liquid water distributions in GDL obtained by X-ray tomography have also been used in some previous works in conjunction with numerical simulations, e.g. Ref. [9]. However, the present work is the first one, to the best of our knowledge, to propose a detailed comparison between PNM simulations and X-ray tomography images of the liquid water distribution in a GDL.

The aim of this article is thus to assess the predictability of pore network and full morphology models to simulate capillarity dominated biphasic flows in GDLs and to study a pore network extraction procedure based on watershed segmentation.

Regarding two-phase flows in GDL, one can distinguish in situ two-phase flows from ex-situ two phase flows. In situ refers to GDL in an operating fuel cell whereas ex situ refers to GDL typically used in characterization experiments involving the sole GDL (as opposed to the GDLs in the membrane electrode assembly (MEA) for the in-situ case). A typical objective of ex-situ experiments is to characterize the capillary pressure curve, an important parameter of the porous media classical two-phase flow model. In situ two-phase flows are a priori more complex than the ones observed in typical ex-situ experiments because of the coupling with heat transfer and the significance of phase change phenomena. Also, obtaining images of in situ liquid distribution from X-ray microscopy is more challenging. For these reasons, it is natural to first develop comparisons between simulations and experiments for the simpler ex-situ conditions. In this paper, an ex-situ configuration is considered.

2. Methodology

2.1. Material

Gas diffusion layer material of the type SGL™ 24BA (SGL Carbon, D) is chosen for this study. SGL™ gas diffusion layer materials are composed from carbon fibers and a micro-porous carbonaceous binder. The pore size of the binder is typically less than 1 μm. SGL™ 24 has an uncompressed thickness of 190 μm and an uncompressed porosity of 84%. The suffix "BA" means that the material is hydrophobized with 5% (w/w) of PTFE and that there is no microporous layer (MPL).

2.2. X-ray tomographic microscopy

Experimental water distributions of a SGL™ 24BA (SGL Carbon, D) gas diffusion layer is determined by X-ray tomographic microscopy. The imaging methodology developed for ex-situ [44,50] and operando environments [47,48] is described in detail in Ref. [49] and is applied to an ex-situ water invasion experiment. Similar set-ups are used in Refs. [23,24]. Throughout the paper, water injection denotes the process in which liquid water is injected into an initially dry capillary structure and gradually invades it.

A circular GDL sample (6 mm in diameter) is placed in the sample holder between two porous membranes. The membrane at the bottom (water side) is hydrophilic whereas the one on top (air side) is hydrophobic. The hydrophilic membrane promotes a

homogeneous water distribution at the bottom side of the GDL. The hydrophobic membrane is used as a barrier for liquid water to gradually saturate the GDL after the breakthrough capillary pressure has been reached (the breakthrough capillary pressure is the minimum pressure between the two fluids, air and water, allowing liquid water to cross the GDL). As discussed in Ref. [49], this choice of synthetic, homogeneous boundary conditions is not representative of in-situ conditions but is well adapted to the determination of the capillary pressure curve. It also simplifies interpretation and modeling studies. The water injection protocol involves a stepwise increase of the liquid pressure. For each imposed liquid pressure, a capillary equilibrium distribution of the liquid water is reached within the GDL. A 3D X-ray tomographic image corresponding to each capillary equilibrium is acquired. Imaging conditions are given in Ref. [49].

Experiments are performed at 25 °C. The voxel size of the 3D image is 2.2 μm. The solid, the liquid and the void phase in the sample are obtained by segmentation of the greyscale image [49]. The voxel resolution of the images does not allow segmenting the pores in the binder of the SGL™ 24BA material. Therefore the binder is considered as a solid. As a consequence the image based porosity of the sample is less than the real porosity.

Global and local saturations can be computed from the images to derive the saturation profile across the GDL thickness and the overall saturation vs. capillary pressure relationship Pc(S). The capillary pressure Pc is the pressure difference between the imposed liquid phase pressure and the gas phase (supposed to be constant and equal to atmospheric pressure). The imaging data are used for comparison with the modeling results.

2.3. Pore network simulations

Pore network simulations have been developed in collaboration between Commissariat à l'Énergie Atomique et aux Énergies Alternatives (CEA) and Institut National Polytechnique de Toulouse (INPT). A pore network is first extracted from the tomographic image of the dry GDL. The extraction procedure is described in the next section. Then the extracted network is used in a Matlab™ pore network code to perform the two-phase simulations. The computed water distributions are displayed and analyzed on images using a mapping between network elements and image regions.

2.3.1. Invasion percolation algorithm

As mentioned before, the GDL pore space is represented as a network of pores and links in the pore network approach. The links represent the constrictions, i.e. the narrower passages between two neighbor pores. Because the GDL is considered as hydrophobic, the water distribution is simulated using the invasion percolation algorithm [9], which is well adapted to describe the very slow displacement of a wetting fluid (the gas phase here) by a non-wetting one (liquid water here). An invasion critical capillary pressure threshold is associated with each link. Physically, this is the maximal value of water pressure the link can hold back (it can be regarded as the link breakthrough pressure). Water invades the GDL one link (and its adjacent pore still free of liquid) after the other, selecting at each step the link on the liquid − gas interface having the lowest invasion critical capillary pressures. This process imitates a quasi-static injection.

2.3.2. Invasion capillary pressure threshold

Each constriction is associated with one critical capillary pressure threshold given by the Young-Laplace equation:

$$P_c = -\frac{2\gamma \cos\theta}{R} \quad (1)$$

where $\gamma = 7.2{*}10^{-2} N.m^{-1}$ is the water/air surface tension at 25 °C, θ is the contact angle and R is the constriction radius.

Constrictions are given as image regions by our pore network extraction procedure. We can thus compute their size on the image. The constriction radius is computed as the size of the largest inscribed ball whose center is located in the constriction.

Modeling the contact angle requires making an assumption. Indeed there are little, if any, detailed experimental data on contact angle heterogeneities within GDLs. Depending on the quality of the hydrophobic treatment or because of aging [51], GDLs can have locally different contact angles. Fine tuning the wettability is an approach to increase GDL performances. However in this work we assumed that the contact angle is uniform. More refined models taking into account variations of the contact angle are left for a future work.

2.3.3. Boundary conditions

In order to impose boundary conditions in the simulations we need to know accurately the location of the elements of the experimental set-up: the GDL, the hydrophobic and hydrophilic membranes and the lateral gasket (Fig. 1). The latest is identified by a cylindrical mask using the software ImageJ [52]. Knowing the shape of the hydrophilic membrane is critical for inlet injection conditions. Hydrophilic and hydrophobic membranes tend to penetrate in the GDL because of the compression. We use a morphological criterion to distinguish between GDL and membranes: GDL fibers are thinner than the membrane. A threshold on the covering radius map is used to set a limit between thin regions and thick ones.

A reservoir inlet boundary condition is applied for the simulation. This means that we assume that the whole inlet face is in contact with a water reservoir at uniform pressure. Because the membrane which is in contact with the inlet face is hydrophilic, the water fills it completely before entering the GDL during the simulations. The interaction of water with the hydrophobic membrane is assumed to be the same as the interaction with the hydrophobic GDL, i.e. we use the same contact angle and water cannot penetrate this membrane. No-flux wall condition is applied between the GDL and the lateral gasket. The water distribution is computed for 5 injection pressures: 14, 22, 28, 39 and 53 mbar.

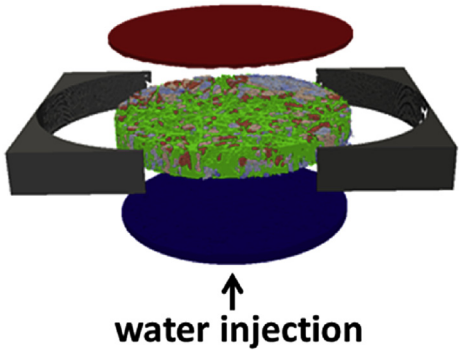

Fig. 1. Experimental set-up elements identified on the image. Green: GDL. Gray: lateral gasket. Blue: hydrophilic membrane. Red: hydrophobic membrane. Colored regions inside the GDL are liquid water at several pressures. (For interpretation of the references to colour in this figure legend, the reader is referred to the web version of this article.)

2.4. Pore network extraction procedure

We develop a pore network extraction method based on watershed segmentation. Our implementation of pore network extraction relies on open sources python libraries such as Scipy and ITK [53,54]. The open source functions used are listed in Table 1.

This section details the steps of the extraction procedure.

2.4.1. Constriction search

It is crucial to identify the constrictions in the pore space in order to model the capillary pressures since the constrictions control the invasions. Indeed, invasion capillary pressure thresholds are the highest where distances between solid parts are the lowest, i.e. at constrictions.

In this work, we define constrictions as being ridges of the distance map. A formal discussion of this definition can be found in Ref. [29]. The geometric reasoning is the following. The distance map is the map giving for each voxel of the pore space the minimum distance to a solid voxel. Fig. 2 illustrates this for a simple 2D geometry. The values in the distance map can be interpreted as depths. The voxels at the edges of the pores have a depth equal to 0 and the points in pores located the farthest from the pore walls correspond to maximum depth points. The center of a constriction is a saddle point, i.e. one can find two paths with an opposite curvature which intersect at this point. Indeed, a longitudinal path, connecting one pore to the pore located across the constriction, reaches its highest point at the constriction center. While a transversal path, connecting one solid edge of the constriction to the opposite solid edge, takes its maximum depth at the constriction center. The constriction is the transversal 2D surface located on the ridge of the distance map. It is also the watershed surface that the watershed algorithm finds.

Watershed segmentation is a common image analysis algorithm, used for example to separate objects at constrictions. Its principle is the following. The distance map is explored starting from marker voxels using a so-called flooding algorithm. Voxels around the markers are in the explored region if they are below a given depth according to the distance map. Then the depth is gradually decreased. Think of it as a flooding of the depth map from the bottom to the top by gradually increasing the water level. When a sufficiently high level is reached, two neighbors regions eventually meet at the ridges of the distance map. So the watershed surfaces search is a two steps process. In the first step markers are defined giving approximate locations of pores. This step is described in the next section. The second step is the ridges search using the flooding algorithm. At the end of this step, watershed surfaces are found between markers. They delimit distinct image regions, the pores. Each pore is then labeled using a connected-component labeling function.

The location and shape of constrictions are thus directly available. Then we can extract the constriction sizes which are directly linked to capillary pressures.

2.4.2. Markers choice

Markers are used to define the approximate location of pores and initialize the watershed segmentation process.

The basic idea is to locate markers at the widest locations (the locations the farthest from pore walls), i.e. at local maxima of the distance map. The problem with taking all local maxima is over-segmentation: the number of local maxima is sensitive to geometry noise like surface roughness. Several approaches have been used to prevent over-segmentation: direct filtering of the distance map [26], pore merging as a post-processing step [29], marker choice based on the medial axis analysis to prevent topology defects [28]. We explore two other methods to reduce the over-segmentation:

- The first method is to impose a minimal distance between two local maxima.
- The second method is to use H-maxima instead of local maxima.

The notion of H-maxima makes it possible to merge local maxima according to a contrast criterion on the distance map [40]. H-maxima are defined as the local maxima of the reconstruction by dilation of the distance map. Reconstruction by dilation [55] is an algorithm which truncates the peaks of the distance map by a height H voxels, so that peaks are replaced by plateaus. The truncation parameter H is a free parameter. Its meaning is the following. Suppose that a noise is superimposed on the distance map, so that the value of each voxel can change by plus or minus H/2. One such noise could come from the stairs-like discretization of surfaces in the image. Then truncating the peaks by H voxels makes it possible to erase the effect of noise on the peaks.

2.4.3. Pores and links connectivity and shape analysis

The connectivity is analyzed after the watershed surfaces are found and the pores are labeled. Each watershed voxel neighborhood is analyzed to list its neighbor pores. Voxels connectivity is defined in this work, so that a voxel is connected with its 26 neighbors voxels, i.e. diagonals included. Watershed voxels having exactly two different neighbor pores are assigned to the link between these two pores. After this analysis, labeled link voxels and connectivity tables between pores and links are available.

The geometry of pores and links are then analyzed. The exact geometry of pores and links is available as voxel regions in the image. Shape descriptors are used to take into account this geometry in the pore network simulations. The shape descriptors we use are the location of the center of mass, the location of the widest point, the inscribed sphere radius and the volume.

Table 1
List of open source functions.

Distance map	SimpleITK.DanielssonDistanceMap
Local maxima search	skimage.feature.peak_local_max
Reconstruction by dilation	skimage.morphology.reconstruction
Watershed search	SimpleITK.MorphologicalWatershedFromMarkers
Connected components labelling	scipy.ndimage.measurements.label
Morphological dilation	SimpleITK.BinaryDilate
Center of mass location	scipy.ndimage.measurement.center_of_mass
Widest point location	scipy.ndimage.measurement.labeled_comprehension (numpy.argmax (distanceMap))
Inscribed sphere radius	scipy.ndimage.measurement.labeled_comprehension (numpy.max (distanceMap))
Volume	scipy.ndimage.measurement.labeled_comprehension (numpy.size)

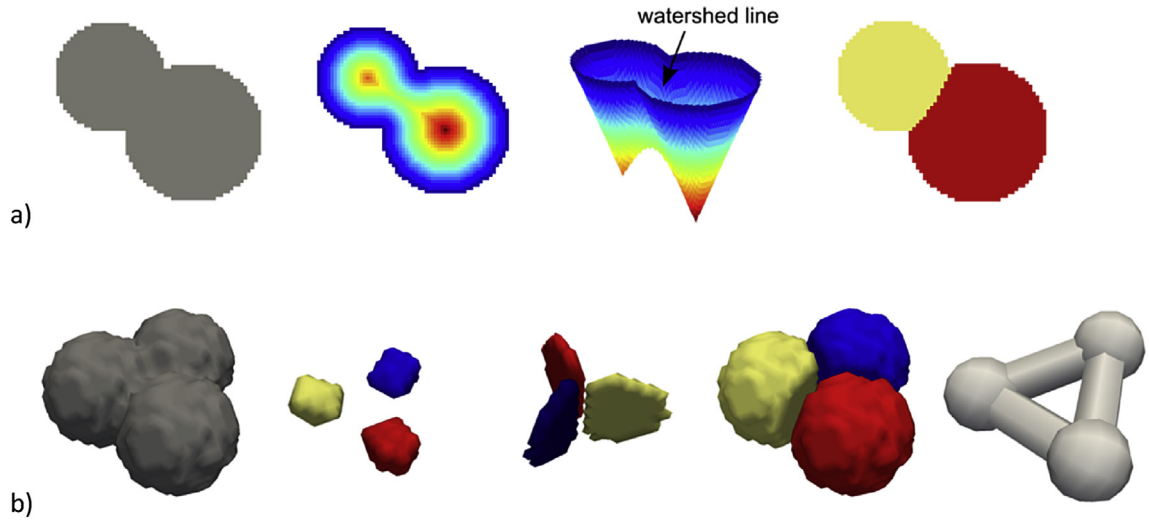

Fig. 2. Watershed segmentation and pore network extraction algorithms illustrated on two simple geometries. a) Watershed segmentation explained on a 2D geometry. From left to right: pore space, distance map, distance map interpreted as a depth map, pores separated by a watershed line. b) Pore network extraction explained on a 3D geometry. From left to right: pore space, markers chosen as H-maxima of the distance map, watershed surfaces, pores separated by watershed surfaces, extracted network.

2.5. Full morphology simulations

In the full morphology simulations, the shape of the region occupied by water is approximated as a union of balls of a constant radius. This is to take into account that all menisci have the same radius under capillary equilibrium condition. Assuming that water has a uniform pressure, that the contact angle is uniform and that menisci are spherical, then the radius is fixed by the Young-Laplace equation. Water invades regions that a ball of radius R can access following a continuous path from the injection points.

Our implementation of the full morphology model is the following. Regions where the distance map is greater than R are selected as ball centers candidates. Centers which are connected to injection points are found using a connected-component labelling algorithm. Non-connected centers are rejected. Then a morphological dilation of radius R is applied to the centers to form water balls.

The open source functions used to implement the full morphology model are listed in Table 1.

2.6. Anisotropy characterization

GDL are anisotropic structures with openings typically greater on average in the in-plane direction compared to the through plane direction. This can have an important consequence on the two-phase flow with the formation of preferential paths in the through plane direction [49]. Characterizing the GDL microstructure anisotropy is therefore of particular interest.

The chord length is a geometric measure which can be used to quantify the geometric anisotropy of regions in a 3D image [56]. Its principle is the following. The intersections of image regions with a series of straight lines parallel to a given direction are computed. These intersection lengths give a measure of the regions size in this direction. By varying the directions of straight lines, we can study the anisotropy of the regions sizes. Implementation details can be found in Ref. [56].

We also characterize the anisotropy of constriction sizes. Our method is as follows. Constrictions are found during the construction of the pores network. The direction of a constriction is computed as the direction of the segment joining the centers of its two neighboring pores. We classify the constrictions in two categories, in-plane and trough-plane, depending on whether they form an angle less than 45° with the through-plane direction. The sizes of constrictions in the in-plane and through-plane directions are compared.

3. Results

3.1. Benchmarking network extraction parameters against full morphology results

As mentioned before pore network extraction from an image is a complex procedure which involves making a choice regarding the definition of pores. We discuss in this section the consequences of the choice of the pore merging parameter. We also suggest that comparing pore network two-phase simulations with full morphology simulations can help verify that the extracted pore network is valid.

The extracted pore network is not unique because the markers choice gives a degree of freedom on pore definition. Two pores can be merged into one or be further divided depending on the markers choice. This degree of freedom is unavoidable because the notion of pore is not uniquely defined. Because there is no absolute criterion to decide whether two pores should be merged or not, the extracted networks are tested from the simulation results they produce rather than from using an intrinsic criterion.

We compare water distributions simulated with the pore network model with those simulated with the full morphology model. Indeed those two simulation methods have many points in common. Capillary forces are computed as a function of radii of maximal ball inscribed in constrictions. The porous medium is invaded from an injection side, the lowest capillary pressure threshold regions first. In the end, provided that boundary conditions are the same, water patterns for a given pressure should be the same.

The main source of information loss between the pore network model and the full morphology model is pore merging because information on the constrictions located inside pores are not taken into account. The possible water bifurcations caused by these constrictions are lost. Thus comparing water patterns given by pore network and full morphology models is one way to assess if a pore network extraction procedure correctly captures the water

bifurcations associated with constrictions.

We use the following quantity to measure the degree of agreement between images of an experimental water distribution and of a numerical water distribution:

$$VoxelMatch(numerical|experimental) = \frac{Sat(numerical \cap experimental)}{Sat(experimental)} \quad (2)$$

where "numerical" and "experimental" denote the voxels filled with water in the two images and Sat is the number of voxels filled with water divided by the total number of pore space voxels, i.e. the overall saturation.

This quantity can be understood as the relative saturation of the numerical water distribution in the experimental water distribution. From a probability point of view, it is also the probability of a voxel to be filled with water in the numerical simulation knowing that it is filled with water in the experimental image. When compared with the overall saturation obtained in the simulation, it gives information on the correlation between the two water distributions. Indeed, the VoxelMatch is one if the two distributions are perfectly correlated. If they are statistically independents, the definition of statistical independence of two events involves the following property:

$$VoxelMatch(numerical|experimental) = Sat(numerical). \quad (3)$$

Thus, the closer to 1 is the VoxelMatch index, the better is the correlation between the experimental and numerical distributions.

Fig. 3 presents the Voxel Match index (Eq. (2)) of pore network water distributions with respect to full morphology water distributions for the five experimental pressures. Several network extraction parameters are benchmarked.

As can be seen from Fig. 3, the least successful choice is to take all local maxima for markers. The voxel match is almost perfect at low pressure, so it indicates that inlet boundary conditions are close. But it decreases as the pressure is increased from 14 mbar to 53 mbar, while the overall saturation increases up to 0.7. This indicates a correlation loss between the results of the two models. This is expected to happen when the impact of constrictions is not taken into account the same way in the two simulation methods. Indeed, let's consider a model of water interacting with random constrictions, as it is the case here where water must choose bifurcations according to constrictions. If constrictions in the two simulations are two uncorrelated random fields, water distributions which are initially correlated because of boundary conditions will lose their correlation because of the impact of different paths taken in the constrictions.

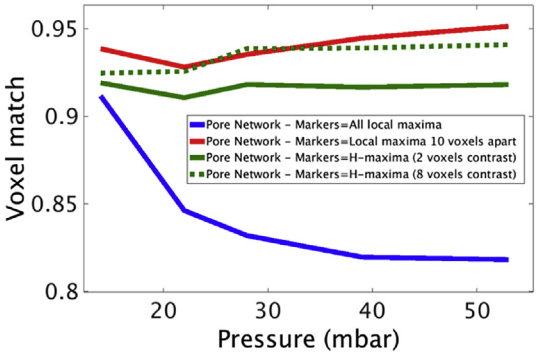

Fig. 3. Voxel matches of pore network water distributions with respect to full morphology water distributions, for 14, 22, 28, 39 and 53 mbar pressures. Simulations are run on the whole GDL sample with uniform wettability $\theta = 115°$.

On the contrary, the pore network and full morphology models give almost the same water distributions with around 95% voxel match when the markers are specified using the H-maxima procedure. This is almost a complete match, as the 5% difference could be explained by the following remarks. Firstly, because the pores are either fully invaded or fully dry in the pore network images, small water regions below the pore scale can differ, such as spherical menisci in full morphology or small roughness which are invaded at high pressure only. Secondly, we left link voxels (1 voxel thick surfaces) blank in PNM images.

This is an interesting result because it shows that these two geometry based methods have the same basis. The full morphology model is completely parameter free, so it can be used to benchmark the pore network complex extraction procedure.

This result also validates the capability of the watershed based extraction procedure to detect constrictions.

Since merging the local maxima clearly increases the match with the full morphology simulations, we recommend using a merging step.

3.2. Comparison between experimental and computed water distributions

We present here a comparison between experimental and computed water distributions. Firstly we look at the voxel by voxel agreement between the water patterns. Secondly we look at the overall saturation and at slice averaged saturation curves. Thirdly we study the water distribution anisotropy using chord length.

3.2.1. Voxel by voxel match

Fig. 4 shows 3D rendering of experimental and simulated water patterns in the whole GDL. We show on the same image the water distribution at several water injection pressure levels: 14, 22, 28, 39 and 53 mbar. The increments in the water presence between one pressure and the next are shown with different colors. Because the water occupied region grows when the pressure is increased, the water distribution at a given pressure is the union of the distributions corresponding to the increments at lower pressures.

Visually, the simulated patterns are close to the experimental ones. The most apparent difference is at the lowest pressure. This probably indicates that the injection conditions are not perfectly well reproduced. The shape of the hydrophilic membrane is probably not sufficiently accurately estimated.

Fig. 5 shows the sample averaged voxel match for the five experimental pressures. It is lowest at low pressure, between 0.4 and 0.6 depending on the simulation method. This noticeable difference with the experiment is probably due to the inlet boundary condition. When increasing pressure the voxel match increases up to 0.8–0.9. This increase is mostly a saturation effect, the average saturation increasing from 0.2 to 0.8. This saturation effect can be evaluated from total saturation levels (shown in dot lines in Fig. 5), representative of the voxel match in the case of statistical independence.

The fact that the voxel match is higher than the total saturation for the middle and high pressures is due to the preservation of initial correlation during the water injection, that is to say the relevance of the capillary model. These results are considered as good since there is only one free parameter, the uniform contact angle. The value $\theta = 115°$ gives the best results. This is consistent with the expected value of contact angle of water on PTFE.

Causes for disagreement are discussed further in the last section.

3.2.2. Averaged saturation curves

A more concise way to characterize the water distributions is to compute the overall saturation and the slice average saturation

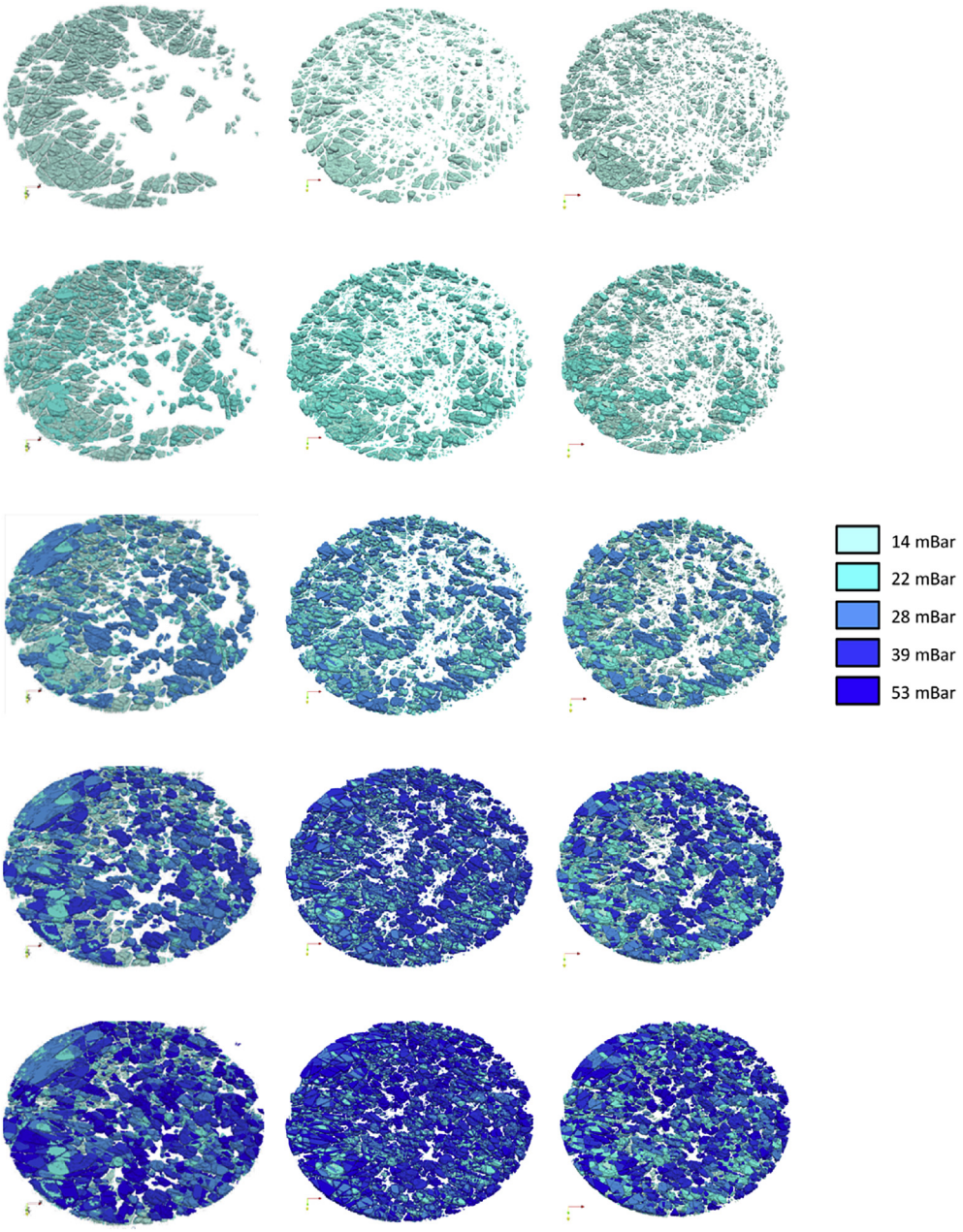

Fig. 4. 3D rendering of water patterns in the GDL at 14, 22, 28, 39 and 53 mbar. From left to right: experiment, full morphology simulation, pore network simulation with H-maxima markers (H-contrast = 8 voxels). Simulations are run on the whole GDL sample with uniform wettability $\theta = 115°$. Each color corresponds to the water distribution increment at a given pressure. (For interpretation of the references to colour in this figure legend, the reader is referred to the web version of this article.)

profile in the through-plane direction for the different pressure levels.

Fig. 6 shows comparisons between the experiment and the simulations as regards the through-plane saturation profiles and the capillary pressure curves. Saturation profiles are x-y slice averaged water saturations as a function of the z-axis, where z is the through plane direction. The five solid line curves represent the simulated saturation profiles at the five experimental pressures. The five dashed lines are the experimental saturation profiles. The capillary pressure curves show the sample averaged saturation as a function of the pressure level. The dashed curves represent the experimental data and the solid curves the simulations. All saturations are computed for the slices 15 to 85. The 0 to 15 slices correspond to the hydrophilic membrane, the 85 to 110 slices to the hydrophobic membrane.

As discussed in Ref. [14], the convex shapes of the experimental saturation profiles at low and middle pressure are different than the ones usually predicted using traditional continuum model based on the generalized Darcy's law and Leverett functions.

The full morphology and pore network simulations both give results quite consistent with the experiment. The capillary pressure curves are almost perfectly reproduced. The global shapes of saturation profiles are also nicely predicted although there remain some inaccuracies regarding the water distribution in the through plane direction. The effect of pressure on saturation profiles is well predicted.

The lowest accuracy was obtained with a pore network extracted without merging the local maxima. Therefore, as in the

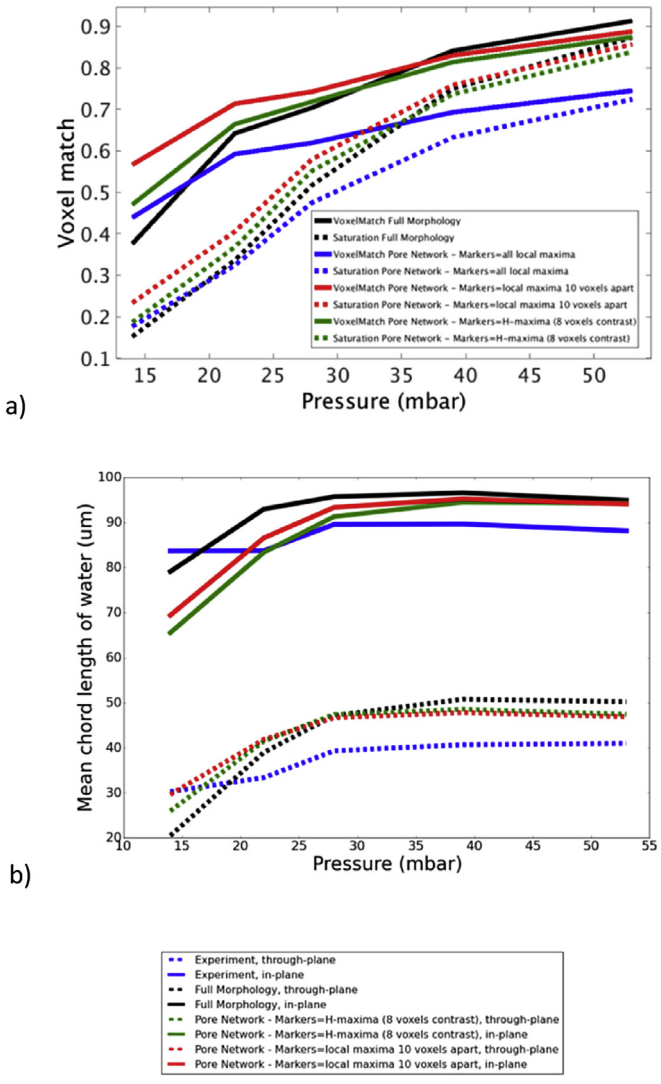

Fig. 5. Quantitative comparison of experimental water distribution with water distribution simulated with full morphology and pore networks. a) Full lines: sample averaged voxel match of simulated water distributions with respect to experimental water distributions. Voxels matches are computed for five pressure levels. Dotted lines: saturation levels of simulations. b) Mean chord lengths of water distributions, as a function of water pressure. Full lines represent in-plane chord lengths, dotted lines represent through-plane chord lengths.

previous section, it is recommended to merge local maxima in the pore network extraction procedure.

3.2.3. Chord lengths

Chord lengths are used to characterize the size of water clusters and the anisotropy. Fig. 5b shows the mean chord lengths of experimental and simulated water distributions.

The mean chord lengths for the experimental water distribution at high capillary pressures are 85 μm in the in-plane direction and 40 μm in the through-plane direction. The mean chord lengths of simulated water distribution are close: 92 μm for in-plane, 48 μm for through-plane. Thus, simulations are able to reproduce the anisotropy. This is another element showing the good match of simulations with the experiment.

The mean chord lengths of the dry pore space are respectively 81 μm and 37 μm. This is not exactly the values found for water distributions, although we could expect that the pore space is filled with water at high pressures. The difference can be explained by the small pores: they reduce the value of the mean chord length of the dry pore space, but not the mean chord length of water. Indeed, small pores are not filled with water, since the GDL is a hydrophobic material.

For comparison, the mean chord lengths of the solid area of the GDL are 74 μm and 33 μm respectively.

3.3. Quantitative analysis of the pore networks

The properties of the extracted networks can be studied in order to compare the extraction procedures. Fig. 7 provides quantitative information on the extracted networks.

The markers selection is a characteristic of our extraction method. The markers choice influences the properties of the resulting networks, such as the number of network elements. Fig. 7a illustrates this point by showing several networks extracted from the same microstructure with different choice of markers. Over-segmentation is illustrated when choosing all the local maxima of the distance map for markers. The number of pores decreases when choosing H-maxima for markers or imposing a minimal distance between markers.

We further characterize the network by the pores sizes distribution, the constrictions sizes distribution, the connectivity (number of neighboring pores of each pore), and the constrictivity (size ratio between neighboring pores and constrictions). Fig. 7b shows these data for three markers choices: no filtration of local maxima, a minimum distance imposed between two markers, and H-maxima.

The pore size distributions (Fig. 7b1) for the “H-maxima” and “unfiltered” networks have shapes reminiscent of the Weibull distribution. This is a standard shape for pore networks. A phenomenon of over-segmentation in the “unfiltered” network can be inferred from the high number of small pores, between 3 and 5 μm. We consider it to be detrimental, because the shape of pores which are only a few voxels wide cannot be precisely resolved. The shape of the pore size distribution obtained with the “minimum distance between markers” network is different from a Weibull distribution. It has two humps, with a cutoff around 3 voxels. This distortion indicates that this marker choice introduces an artificial cutoff between small pores and large pores.

Constriction size distributions (Fig. 7b.2) have similar shapes for the different networks. The distribution of links between the in-plane and the through-plane categories is as follows: 16% of constrictions are through-plane for the “unfiltered” network, 8% for the “minimum distance between markers” network, 10% for the “H-maxima” network. Overall, the through-plane sizes are close to the in-plane sizes, except for more frequent through-plane constrictions between 5 and 8 μm in the “minimum distance between markers” network. However, the pore space was found to be anisotropic in Ref. [49], using the notion of continuous pore size distribution [57]. More precise analysis of the constrictions geometry might be necessary in order to ascertain the anisotropy of constrictions.

Fig. 7b.3 shows the connectivity distributions. The “unfiltered” network has greater connectivity than other networks. This can be explained by the over-segmentation. The “H-maxima” network has fewer pores with 1 neighbor only compared to the “minimum distance between markers” network. It is considered positive because the pores with only one neighbor make inert dead-ends.

The constrictivity distributions are shown in Fig. 7b.4. For the “unfiltered” network, the most common ratio between pore radius and constriction radius, is 1. This is considered detrimental, because the constrictions are expected to be smaller than the pores. It is an indication of over-segmentation. As stated in Section 2.4.2, in the “H-maxima” network a constriction width is lower than the width

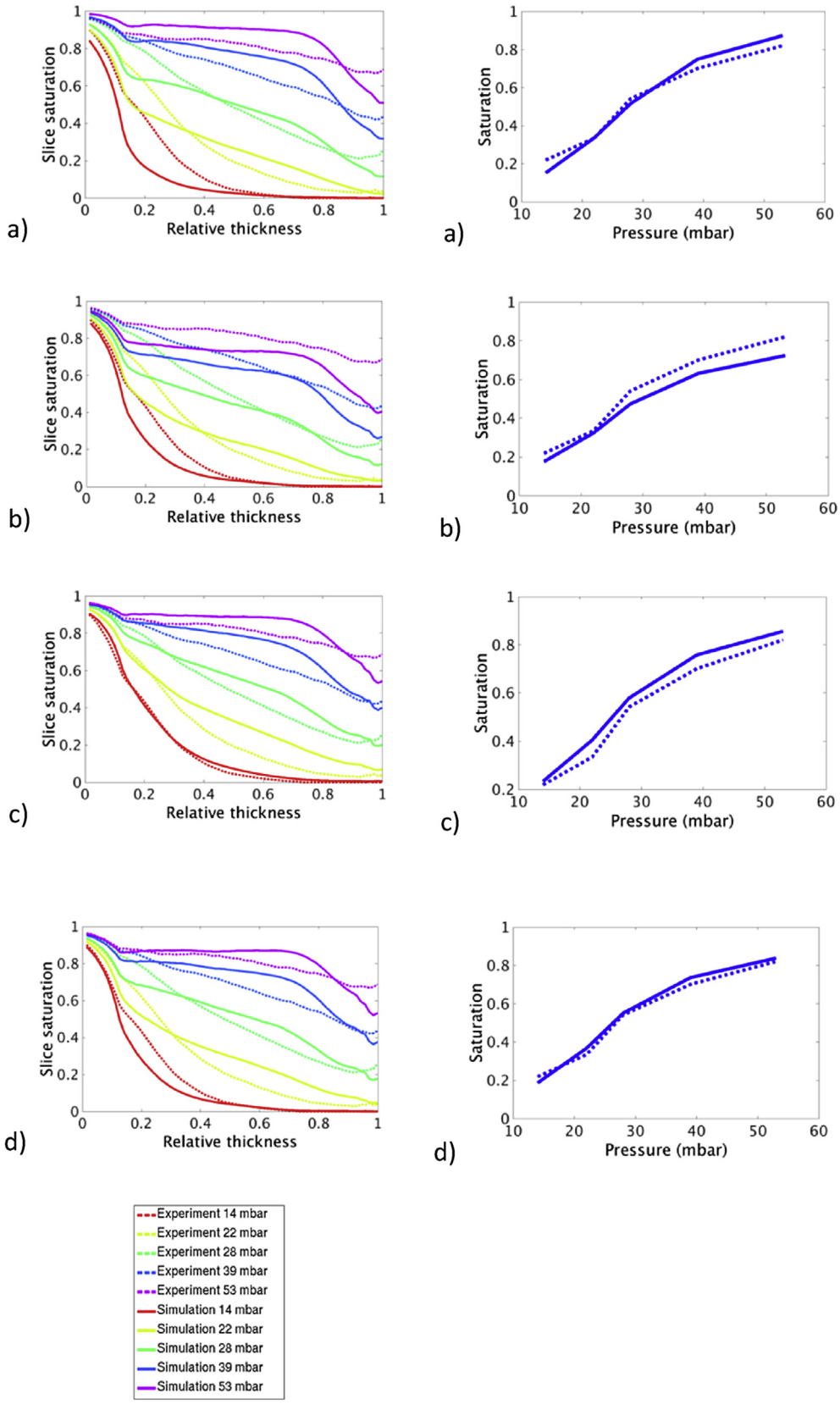

Fig. 6. Averaged saturations of simulated water distributions compared with experimental ones. Left: saturation profiles in the through-plane direction. Experimental curves are in dotted lines, simulations curves are in full lines. Right: capillary pressure curves. Simulation methods: a) Full morphology b) Pore network, markers = all local maxima c) Pore network, markers = local maxima at least 10 voxels apart, d) Pore network, markers = H-maxima (H-contrast = 8 voxels). Simulations are run on the whole GDL sample with uniform wettability θ=115°.

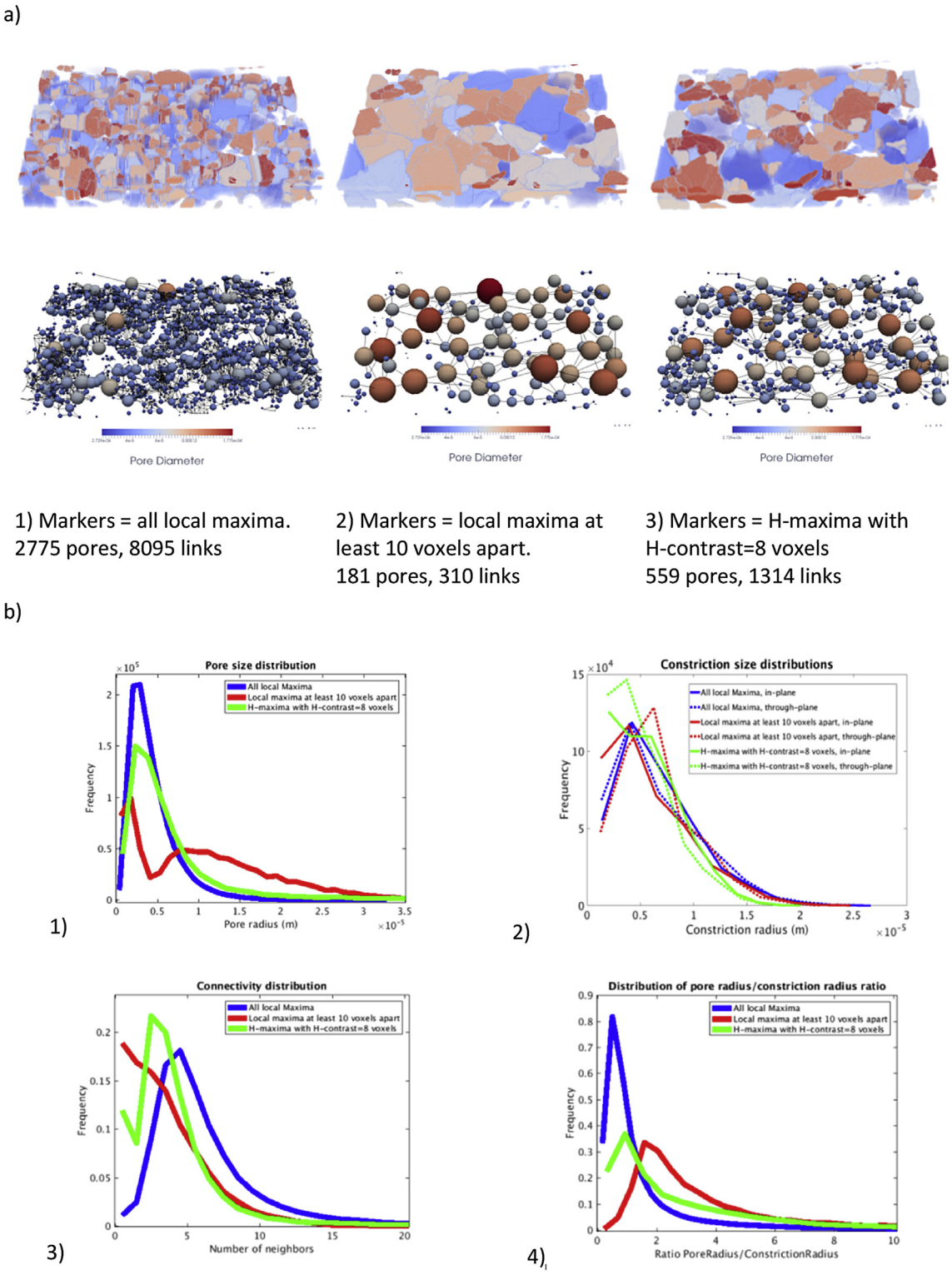

Fig. 7. Pore network extracted from a GDL subsample. a) 3D rendering of pores (top) and networks (bottom). Network elements are displayed with reduced size to increase readability. Criteria for markers choice are, from left to right a.1) all local maxima, a.2) local maxima at least 10 voxels apart, a.3) H-maxima with H-contrast = 8 voxels. b) Quantitative data on the pore network. b.1) Pore size distributions. b.2) Constriction size distributions, in-plane and through-plane. b.3) Connectivity distribution. b.4) Constrictivity distribution.

of the smallest of its two neighboring pores minus H voxels. This relationship between pore size and constrictivity could explain why the constrictivity distribution of the "H-maxima" network has a shape similar to the shape of the pore size distribution.

3.4. Computation performances

The number of voxels in the tomography image is around 700 millions. Extracting the pore network from such an image takes

40 min and 40 Gb Ram on one Intel Xeon 5 2.2 Ghz CPU. Pore network simulations on the extracted pore network take 1 min. Full morphology simulations for the five pressure levels take 25 min.

4. Discussion

The agreement between the experiments and the simulations is considered as good but is not perfect. Possible model improvements are briefly discussed in this section.

Uncertainties regarding the inlet conditions are considered as a major cause of discrepancies between the simulations and the experiment. In this work we imposed inlet boundary conditions considering the hydrophilic membrane as a water reservoir. Accordingly, water enters the GDL where the fibers in contact with the membrane correspond to the lowest capillary pressure threshold. This method does not give a good accuracy on the water distribution near the hydrophilic membrane because it is too sensitive to the membrane geometry which is difficult to distinguish from the GDL. Another approach would be to use experimental water locations near the hydrophilic membrane, at the lowest pressure level, to define injection points and thus the initial conditions for the simulation. It boils down to simulating a water increment knowing the previous water distribution, in order not to be disturbed by injection conditions.

The capillary model could be improved taking into account the possible wettability heterogeneities. Curved menisci are visible in the experimental water images. The constriction size at the menisci may give an indication on the local contact angles using (Eq. (1)). These contact angles could be used as input for the pore network simulations. Another approach would be to estimate local contact angles from a model mixing fibers and binder contact angles. Assuming that fibers and binder could be distinguished on the image, the pore network extraction procedure makes it possible to extract the chemical composition, i.e. fiber or binder, of the vicinity of each constriction from the images.

GDL constrictions in the in-plane direction are more elongated than in the through plane direction. Inscribed balls radii do not take properly this effect into account. A better estimator of the invasion capillary pressure threshold in elongated constrictions is the hydraulic radius [58,59].

We recommended using a pore merging procedure before the watershed segmentation in order to prevent over-segmentation. Further studies are needed to check whether the H-maxima procedure recommended in our paper also apply to other fibrous materials than the GDL SGL™ 24BA.

5. Conclusion

Pore network and full morphology simulations of quasi-static two-phase flow in a gas diffusion layer were performed. A pore network extraction method based on watershed segmentation was developed. The geometry of the tomographic image was analyzed to identify pores and constrictions. A comparison between full morphology and pore network two-phase simulations was performed. This validated the extraction procedure. The extraction computations are fast (40min for a 700 million voxels image) and were developed using open source libraries. Hence the comparison with the full morphology approach provides a way to optimally specify the pore network extraction parameters and make the pore network approach more predictive than when only the microstructure is available.

Tomographic microscopy images of water imbibition into a GDL material (SGL™ 24BA) were used as reference data for comparison with numerical simulations. Full morphology and pore network simulations produced capillary pressure curves and saturation profiles reasonably similar to the experimental data. The results were obtained using a uniform wettability assumption. The voxel by voxel agreement between the experimental and simulated water distributions was analyzed. It also showed a good overall agreement. Experimental and modeling uncertainties were discussed to explain the remaining discrepancies between the experimental and numerical results.

Even if some improvements in the modeling are still desirable, the main conclusion is that full morphology and image based pore network models are quite reliable methods to simulate water distributions in GDLs. This is good news since pore network models have been used in many previous investigations to simulate two-phase flows in ex-situ as well as in-situ GDLs and will certainly be used in future work. They permit computationally cheaper and faster simulations than direct simulations and are more appropriate than continuum models because a GDL is a thin porous medium with very few pores over its thickness, thus characterized by a lack of length scale separation between the pore scale and the sample scale.

One can wonder, however, why developing pore network models since practically identical results are obtained with the full morphology model with fewer assumptions. A first point is that the pore network simulations are faster (not considering the pore network extraction step but only the two phase flow simulations). More importantly, pore network models make it possible to simulate more advanced biphasic phenomena than the full morphology model, such as for instance two-phase flows in systems of mixed wettability or in the presence of viscous effects for instance. From a more general point of view, the present work shows that pore network models are well adapted to simulate two-phase flow, at least in the quasi-static limit only considered in the present work and in fibrous materials: an important class of materials encountered not only in fuel cells but also in many other applications such as filter media and dewatering felt. It should be emphasized that the applicability of pore network modeling to this particular class of porous systems has frequently been a subject of questions owing to the particular features of fibrous media microstructures. It was by no means obvious that a technique developed initially for simulating two-phase flows in porous rocks and granular materials is also applicable to fibrous media.

This work opens up the route to model real structures with image based pore networks with consideration of more complex but more realistic in situ processes such as evaporation and condensation and to derive effective properties as a function of GDL local properties (structure, wettability) which will be important steps to analyze the influence of modifications of GDL and thus suggest design recommendations.

Acknowledgements

The authors gratefully acknowledge the funding from the EU project IMPALA ("IMprove Pemfc with Advanced water management and gas diffusion Layers for Automotive application", project number: 303446) within the Fuel Cells and Hydrogen Joint Undertaking (FCHJU), and SGL Carbon for the supply with gas diffusion layer materials.

References

[1] L. Cindrella, A.M. Kannan, J.F. Lin, K. Saminathan, Y. Ho, C.W. Lin, et al., Gas diffusion layer for proton exchange membrane fuel cells—A review, J. Power Sources 194 (2009) 146–160, http://dx.doi.org/10.1016/j.jpowsour.2009.04.005.

[2] B. Straubhaar, J. Pauchet, M. Prat, Water transport in gas diffusion layer of a polymer electrolyte fuel cell in the presence of a temperature gradient. Phase change effect, Int. J. Hydrogen Energy 40 (2015) 2–9, http://dx.doi.org/

10.1016/j.ijhydene.2015.04.027.
[3] P.P. Mukherjee, Q. Kang, C.-Y. Wang, Pore-scale modeling of two-phase transport in polymer electrolyte fuel cells—progress and perspective, Energy Environ. Sci. 4 (2011) 346–369, http://dx.doi.org/10.1039/b926077c.
[4] H.-J. Vogel, J. Tölke, V.P. Schulz, M. Krafczyk, K. Roth, Comparison of a lattice-Boltzmann model, a full-morphology model, and a pore network model for determining capillary pressure–saturation relationships, Vadose Zo. J. 4 (2005) 380, http://dx.doi.org/10.2136/vzj2004.0114.
[5] V.P. Schulz, J. Becker, A. Wiegmann, P.P. Mukherjee, C.-Y. Wang, Modeling of two-phase behavior in the gas diffusion medium of PEFCs via full morphology approach, J. Electrochem. Soc. 154 (2007) B419, http://dx.doi.org/10.1149/1.2472547.
[6] M.J. Blunt, M.D. Jackson, M. Piri, P.H. Valvatne, Detailed physics, predictive capabilities and macroscopic consequences for pore-network models of multiphase flow, Adv. Water Resour. 25 (2002) 1069–1089, http://dx.doi.org/10.1016/S0309-1708(02)00049-0.
[7] M. Blunt, Flow in porous media—pore-network models and multiphase flow, Curr. Opin. Colloid Interface Sci. 6 (2001) 197–207, http://dx.doi.org/10.1016/S1359-0294(01)00084-X.
[8] J. Hinebaugh, A. Bazylak, Pore network modeling to study the effects of common assumptions in GDL liquid water invasion studies, in: ASME 2012 10th Int. Conf. Fuel Cell Sci. Eng. Technol., ASME, 2012, pp. 479–484, http://dx.doi.org/10.1115/FuelCell2012-91466.
[9] O. Chapuis, M. Prat, M. Quintard, E. Chane-Kane, O. Guillot, N. Mayer, Two-phase flow and evaporation in model fibrous media, J. Power Sources 178 (2008) 258–268, http://dx.doi.org/10.1016/j.jpowsour.2007.12.011.
[10] J.T. Gostick, M.A. Ioannidis, M.W. Fowler, M.D. Pritzker, Pore network modeling of fibrous gas diffusion layers for polymer electrolyte membrane fuel cells, J. Power Sources 173 (2007) 277–290, http://dx.doi.org/10.1016/j.jpowsour.2007.04.059.
[11] J. Hinebaugh, Z. Fishman, A. Bazylak, Unstructured pore network modeling with heterogeneous PEMFC GDL porosity distributions, J. Electrochem. Soc. 157 (2010) B1651, http://dx.doi.org/10.1149/1.3486095.
[12] B. Markicevic, A. Bazylak, N. Djilali, Determination of transport parameters for multiphase flow in porous gas diffusion electrodes using a capillary network model, J. Power Sources 171 (2007) 706–717, http://dx.doi.org/10.1016/j.jpowsour.2007.06.053.
[13] G. Luo, Y. Ji, C.-Y. Wang, P.K. Sinha, Modeling liquid water transport in gas diffusion layers by topologically equivalent pore network, Electrochim. Acta 55 (2010) 5332–5341, http://dx.doi.org/10.1016/j.electacta.2010.04.078.
[14] M. Rebai, M. Prat, Scale effect and two-phase flow in a thin hydrophobic porous layer. Application to water transport in gas diffusion layers of proton exchange membrane fuel cells, J. Power Sources 192 (2009) 534–543, http://dx.doi.org/10.1016/j.jpowsour.2009.02.090.
[15] S.P. Kuttanikkad, M. Prat, J. Pauchet, Pore-network simulations of two-phase flow in a thin porous layer of mixed wettability: application to water transport in gas diffusion layers of proton exchange membrane fuel cells, J. Power Sources 196 (2011) 1145–1155, http://dx.doi.org/10.1016/j.jpowsour.2010.09.029.
[16] R. Wu, Q. Liao, X. Zhu, H. Wang, Impacts of the mixed wettability on liquid water and reactant gas transport through the gas diffusion layer of proton exchange membrane fuel cells, Int. J. Heat. Mass Transf. 55 (2012) 2581–2589, http://dx.doi.org/10.1016/j.ijheatmasstransfer.2012.01.002.
[17] P.K. Sinha, C.-Y. Wang, Liquid water transport in a mixed-wet gas diffusion layer of a polymer electrolyte fuel cell, Chem. Eng. Sci. 63 (2008) 1081–1091, http://dx.doi.org/10.1016/j.ces.2007.11.007.
[18] K.J. Lee, J.H. Kang, J.H. Nam, Liquid water distribution in hydrophobic gas-diffusion layers with interconnect rib geometry: an invasion-percolation pore network analysis, Int. J. Hydrogen Energy 39 (2014) 6646–6656, http://dx.doi.org/10.1016/j.ijhydene.2014.01.206.
[19] K.J. Lee, J.H. Nam, C.J. Kim, Steady saturation distribution in hydrophobic gas-diffusion layers of polymer electrolyte membrane fuel cells: a pore-network study, J. Power Sources 195 (2010) 130–141, http://dx.doi.org/10.1016/j.jpowsour.2009.06.076.
[20] K.-J. Lee, J.H. Nam, C.-J. Kim, Pore-network analysis of two-phase water transport in gas diffusion layers of polymer electrolyte membrane fuel cells, Electrochim. Acta 54 (2009) 1166–1176, http://dx.doi.org/10.1016/j.electacta.2008.08.068.
[21] P.K. Sinha, C.-Y. Wang, Pore-network modeling of liquid water transport in gas diffusion layer of a polymer electrolyte fuel cell, Electrochim. Acta 52 (2007) 7936–7945, http://dx.doi.org/10.1016/j.electacta.2007.06.061.
[22] E.F. Médici, J.S. Allen, Evaporation, two phase flow, and thermal transport in porous media with application to low-temperature fuel cells, Int. J. Heat. Mass Transf. 65 (2013) 779–788, http://dx.doi.org/10.1016/j.ijheatmasstransfer.2013.06.035.
[23] P.A. García-Salaberri, G. Hwang, M. Vera, A.Z. Weber, J.T. Gostick, Effective diffusivity in partially-saturated carbon-fiber gas diffusion layers: effect of through-plane saturation distribution, Int. J. Heat. Mass Transf. 86 (2015) 319–333, http://dx.doi.org/10.1016/j.ijheatmasstransfer.2015.02.073.
[24] I.V. Zenyuk, D.Y. Parkinson, G. Hwang, A.Z. Weber, Electrochemistry Communications Probing water distribution in compressed fuel-cell gas-diffusion layers using X-ray computed tomography, Electrochem. Commun. 53 (2015) 24–28.
[25] H. Dong, M.J. Blunt, Pore-network extraction from micro-computerized-tomography images, Phys. Rev. E - Stat. Nonlinear, Soft Matter Phys. 80 (2009) 1–11, http://dx.doi.org/10.1103/PhysRevE.80.036307.
[26] A. Rabbani, S. Jamshidi, S. Salehi, An automated simple algorithm for realistic pore network extraction from micro-tomography images, J. Pet. Sci. Eng. 123 (2014) 164–171, http://dx.doi.org/10.1016/j.petrol.2014.08.020.
[27] D. Wildenschild, A.P. Sheppard, X-ray imaging and analysis techniques for quantifying pore-scale structure and processes in subsurface porous medium systems, Adv. Water Resour. 51 (2013) 217–246, http://dx.doi.org/10.1016/j.advwatres.2012.07.018.
[28] A.P. Sheppard, R.M. Sok, H. Averdunk, Improved pore network extraction methods, in: Int. Symp. Soc. Core Anal., 2005, pp. 1–11 doi:SCA2005-20.
[29] U. Homberg, D. Baum, S. Prohaska, U. Kalbe, K.J. Witt, Automatic extraction and analysis of realistic pore structures from μ CT data for pore space characterization of graded soil, in: Int. Conf. Scour Erosi, Paris, 2012, pp. 345–352.
[30] J.Y. Arns, A.P. Sheppard, C.H. Arns, M.A. Knackstedt, A. Yelkhovsky, W.V. Pinczewski, Pore-level validation of representative pore networks obtained from micro-ct images, in: Proc. Int. Symp. Soc. Core Anal., 2007, pp. 1–12.
[31] P. Bhattad, C.S. Willson, K.E. Thompson, Effect of network structure on characterization and flow modeling using x-ray micro-tomography images of granular and fibrous porous media, Transp. Porous Media 90 (2011) 363–391, http://dx.doi.org/10.1007/s11242-011-9789-7.
[32] N.A. Idowu, C. Nardi, H. Long, T. Varslot, P.E. Øren, Effects of segmentation and skeletonisation algorithms on pore networks and predicted multiphase transport properties on reservoir rock samples, in: SPE Reserv. Characterisation Simul. Conf. Exhib., vol. 17, 2013, pp. 1–13.
[33] H. Dong, S. Fjeldstad, S. Roth, S. Bakke, P. Øren, Pore network modelling on carbonate: a comparative study of different micro-CT network extraction methods, in: Proc. Int. Symp. Soc. Core Anal., 2008, pp. 2008–2031.
[34] J. Roerdink, A. Meijster, The watershed transform: definitions, algorithms and parallelization strategies, Fundam. Inf. 41 (2000) 187–228, http://dx.doi.org/10.3233/FI-2000-411207.
[35] F. Meyer, The Watershed Concept and its Use in Segmentation: a Brief History, 2012. http://arxiv.org/abs/1202.0216.
[36] K.E. Thompson, C.S. Willson, W. Zhang, Quantitative computer reconstruction of particulate materials from microtomography images, Powder Technol. 163 (2006) 169–182, http://dx.doi.org/10.1016/j.powtec.2005.12.016.
[37] R.A. Ketcham, Computational methods for quantitative analysis of three-dimensional features in geological specimens, Geosphere 1 (2005) 32–41, http://dx.doi.org/10.1130/GES00001.1.
[38] I.-M. Sintorn, S. Svensson, M. Axelsson, Segmentation of individual pores in 3D paper images, Nord. Pulp Pap. Res. J. 20 (2005) 316–319.
[39] R.C. Atwood, J.R. Jones, P.D. Lee, L.L. Hench, Analysis of pore interconnectivity in bioactive glass foams using X-ray microtomography, Scr. Mater 51 (2004) 1029–1033, http://dx.doi.org/10.1016/j.scriptamat.2004.08.014.
[40] A. Amankwah, C. Aldrich, Rock image segmentation using watershed with shape markers, in: 2010 IEEE 39th Appl. Imag. Pattern Recognit. Work, IEEE, 2010, pp. 1–7, http://dx.doi.org/10.1109/AIPR.2010.5759719.
[41] K. Thompson, C. Willson, C. White, S. Nyman, J. Bhattacharya, A. Reed, Application of a new grain-based reconstruction algorithm to micro-tomography images for quantitative characterization and flow modeling, SPE J. 13 (2008) 164–176, http://dx.doi.org/10.2118/95887-PA.
[42] A.P. Sheppard, R.M. Sok, H. Averdunk, V.B. Robins, A. Ghous, Analysis of rock microstructure using high- resolution x-ray tomography, in: Proc. Int. Symp. Soc. Core Anal., 2006, pp. 1–12.
[43] Bazylak, Liquid water visualization in PEM fuel cells: a review, Int. J. Hydrogen Energy 34 (2009) 3845–3857, http://dx.doi.org/10.1016/j.ijhydene.2009.02.084.
[44] R. Flückiger, F. Marone, M. Stampanoni, A. Wokaun, F.N. Büchi, Investigation of liquid water in gas diffusion layers of polymer electrolyte fuel cells using X-ray tomographic microscopy, Electrochim. Acta 56 (2011) 2254–2262, http://dx.doi.org/10.1016/j.electacta.2010.12.016.
[45] J. Gostick, H. Gunterman, B. Kienitz, Tomographic imaging of water injection and withdrawal in PEMFC gas diffusion layers, ECS Trans. 33 (2010) 1407–1412, http://dx.doi.org/10.1149/1.3484632.
[46] H. Markötter, I. Manke, P. Krüger, T. Arlt, J. Haussmann, M. Klages, et al., Investigation of 3D water transport paths in gas diffusion layers by combined in-situ synchrotron X-ray radiography and tomography, Electrochem. Commun. 13 (2011) 1001–1004, http://dx.doi.org/10.1016/j.elecom.2011.06.023.
[47] T. Rosen, J. Eller, J. Kang, N.I. Prasianakis, J. Mantzaras, F.N. Buchi, Saturation dependent effective transport properties of PEFC gas diffusion layers, J. Electrochem. Soc. 159 (2012) F536–F544, http://dx.doi.org/10.1149/2.005209jes.
[48] I. Mayrhuber, F. Marone, M. Stampanoni, T.J. Schmidt, F.N. Buechi, Fast x-ray tomographic microscopy: investigating mechanisms of performance drop during freeze starts of polymer electrolyte fuel cells, ChemElectroChem. 2 (10) (2015) 1551–1559, http://dx.doi.org/10.1002/celc.201500132.
[49] A. Lamibrac, J. Roth, M. Toulec, F. Marone, M. Stampanoni, F. Buechi, Characterization of liquid water saturation in gas diffusion layers by x-ray tomographic microscopy, J. Electrochem. Soc. 163 (2016) F202–F209.
[50] J. Becker, R. Flückiger, M. Reum, F.N. Büchi, F. Marone, M. Stampanoni, Determination of material properties of gas diffusion layers: experiments and simulations using phase contrast tomographic microscopy, J. Electrochem. Soc. 156 (2009) B1175, http://dx.doi.org/10.1149/1.3176876.
[51] J. Pauchet, M. Prat, P. Schott, S.P. Kuttanikkad, Performance loss of proton exchange membrane fuel cell due to hydrophobicity loss in gas diffusion

layer: analysis by multiscale approach combining pore network and performance modelling, Int. J. Hydrogen Energy 37 (2012) 1628–1641, http://dx.doi.org/10.1016/j.ijhydene.2011.09.127.
[52] C.A. Schneider, W.S. Rasband, K. Eliceiri, NIH Image to ImageJ: 25 years of image analysis, Nat. Methods 9 (2012) 671–675.
[53] B.C. Lowekamp, D.T. Chen, L. Ibáñez, D. Blezek, The design of SimpleITK, Front. Neuroinform. 7 (2013) 45, http://dx.doi.org/10.3389/fninf.2013.00045.
[54] R. Beare, R. Beare, G. Lehmann, G. Lehmann, The watershed transform in ITK - discussion and new developments, Insight J. (2006) 1–24. http://hdl.handle.net/1926/202.
[55] L. Vincent, Morphological grayscale reconstruction in image analysis: applications and efficient algorithms, IEEE Trans. Image Process 2 (1993) 633–635, http://dx.doi.org/10.1109/83.217222.
[56] P.A. García-Salaberri, J.T. Gostick, G. Hwang, A.Z. Weber, M. Vera, Effective diffusivity in partially-saturated carbon-fiber gas diffusion layers: effect of local saturation and application to macroscopic continuum models, J. Power Sources 296 (2015) 440–453, http://dx.doi.org/10.1016/j.jpowsour.2015.07.034.
[57] B. Münch, L. Holzer, Contradicting geometrical concepts in pore size analysis attained with electron microscopy and mercury intrusion, J. Am. Ceram. Soc. 91 (2008) 1551–2916.
[58] W.B. Lindquist, The geometry of primary drainage, J. Colloid Interface Sci. 296 (2006) 655–668, http://dx.doi.org/10.1016/j.jcis.2005.09.041.
[59] P.-E. Oren, S. Bakke, O.J. Arntzen, Extending predictive capabilities to network models, SPE J. 3 (1998) 324–336, http://dx.doi.org/10.2118/52052-PA.